ACS APPLIED ENERGY MATERIALS

www.acsaem.org

Forum Article

Discovery of n-Type Zintl Phases $RbAlSb_4$, $RbGaSb_4$, $CsAlSb_4$, and $CsGaSb_4$

Brenden R. Ortiz,* Prashun Gorai, Tara Braden, Erik A. Bensen, Stephen D. Wilson, Vladan Stevanović, and Eric S. Toberer*

Cite This: *ACS Appl. Energy Mater.* 2020, 3, 2182–2191

Read Online

ACCESS | Metrics & More | Article Recommendations | Supporting Information

ABSTRACT: Zintl phases are excellent candidates for high-efficiency thermoelectrics (TEs) due to their extremely low lattice thermal conductivity. The manufacturing of an all-Zintl module is particularly attractive for practical applications, as it alleviates concerns regarding the electronic, thermal, and mechanical compatibility of the p- and n-type legs. To date, a large majority of Zintl phases have been realized as p-type TE materials. Our recent discovery of n-type transport in Ba-doped $KAlSb_4$ and $KGaSb_4$ has helped demonstrate the potential of n-type Zintl thermoelectrics. In this paper, we report the experimental discovery of 4 ABX_4 Zintl phases: $RbAlSb_4$, $RbGaSb_4$, $CsAlSb_4$, and $CsGaSb_4$. Transport measurements on Ba-doped $RbGaSb_4$ and $CsGaSb_4$ demonstrate near glassy lattice thermal conductivity (<0.5 W m^{-1} K^{-1}, 350 °C) and lightly doped n-type transport. However, the doping efficiency of Ba in $RbGaSb_4$ and $CsGaSb_4$ is significantly impeded when compared to our prior work on $KGaSb_4$. To investigate the underlying mechanism, we performed first-principles defect calculations and found that the effect of compensating alkali metal vacancies increases in the Rb- and Cs-based analogues. Considering the TE potential of the known ABX_4 n-type materials, we have also performed a computational survey over 27 plausible compositions where A = (K, Rb, Cs), B = (Al, Ga, In), and X = (As, Sb, Bi) to investigate the effect of chemistry on potential TE performance.

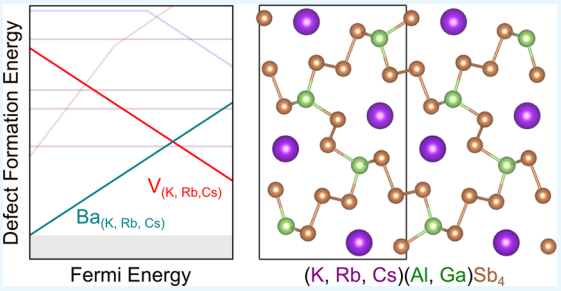

KEYWORDS: *n-type Zintl, n-type thermoelectric, defect calculations, doping*

INTRODUCTION

The discovery of high-performance thermoelectric materials is a complex process, due in part to the interdependent nature of electron and phonon transport processes.[1] The same scattering phenomena that create low thermal conductivity often hinder electronic transport and force a reduction in the electronic mobility. A long-standing challenge in thermoelectrics is the discovery of materials that circumvent this paradigm. In this respect, the Zintl phases are uniquely suited for thermoelectric applications.[2−4] Despite inherently low (near glassy) lattice thermal conductivity, Zintls often maintain respectable electronic transport. Such a unique prospect has even prompted the concept of the phonon-glass electron-crystal (PGEC) concept within thermoelectrics.[5]

Zintl phases have been recognized as a promising class of thermoelectric materials since the 1990s. Many technologically relevant thermoelectrics are Zintl phases, whose structural diversity can range from the clathrates (e.g., $Ba_8Ga_{16}Ge_{30}$),[6−15] interstitially filled skutterudites (e.g., $CeCo_4Sb_{12}$)[16−25] and complex rare-earth/alkali-earth-containing networks (e.g., $Yb_{14}MnSb_{11}$).[26−36] The continued success of these materials has culminated in the development of Zintl-based radioisotope thermoelectric generators (RTG) for deep-space power applications.[37] However, the design of effective and reliable modules depends heavily on the chemical, mechanical, and electrical compatibility of the different thermoelectric segments. A persistent problem has been the relative scarcity of n-type Zintl compounds, as the vast majority of Zintl materials present as p-type semiconductors. Computational searches for high-efficiency n-type thermoelectric materials have historically neglected dopability metrics. Subsequently, computational predictions have often been challenging to realize experimentally (e.g., LiZnSb).[38,39] Recent computational studies even suggest that the majority of the well-studied Zintl phases may be fated to exhibit p-type transport regardless of doping or growth conditions.[40] Even the advent of phase-boundary mapping[41−44] may be powerless to realize equilibrium n-type transport in many of the Zintl materials due to the facile formation of alkali and alkali earth metal vacancies. The development of n-type Mg_3Sb_2 is the most successful counterpoint, wherein Mg-rich conditions enabled n-type

Special Issue: Thermoelectrics

Received: January 10, 2020
Accepted: February 20, 2020
Published: February 20, 2020

https://dx.doi.org/10.1021/acsaem.0c00048
ACS Appl. Energy Mater. 2020, 3, 2182–2191

transport in a historically p-type semiconductor.[42] However, there is considerable debate as to whether Mg_3Sb_2 is a Zintl phase.[45] Thus, until recently, high-efficiency n-type Zintl thermoelectrics were largely restricted to the clathrates and skutterudites. Our discovery of n-type transport and good performance ($zT \sim 1$, 350−400 °C) in Ba-doped $KAlSb_4$ and Ba-doped $KGaSb_4$ helped to demonstrate the potential of other n-type Zintl phases.[46,47] Despite being discovered in the early 1990s, these materials had seen little characterization efforts beyond X-ray diffraction.[49,50]

In this work, we present the experimental discovery of four new Zintl materials, $RbAlSb_4$, $RbGaSb_4$, $CsAlSb_4$, and $CsGaSb_4$. The materials were synthesized as polycrystalline powders and characterized via high-resolution synchrotron X-ray diffraction. Structures were solved from the powder patterns using charge flipping methods and were found to be isostructural to $KAlSb_4$ and $KGaSb_4$. Rietveld refinements allowed us to compare structural trends between ABX_4 compounds with varying alkali (K, Rb, Cs) and group 13 (Al, Ga) atoms. For transport measurements, we chose to concentrate on the Ga-series of compounds, although we expect results to generalize to the Al-based analogues. Similar to our work on $KGaSb_4$, we doped samples of $KGaSb_4$, $RbGaSb_4$, and $CsGaSb_4$ with 2.5% Ba, finding that all materials are n-type dopable. However, the Hall carrier concentration decreases significantly between $KGaSb_4$ (10^{19} e^- cm^{-3}), $RbGaSb_4$ (10^{18} e^- cm^{-3}), and $CsGaSb_4$ (10^{17} e^- cm^{-3}). Subsequent density functional theory calculations reveal that the formation of compensating alkali metal vacancies becomes increasingly favorable as the alkali metal transitions from K, Rb, and Cs, corroborating experimental Hall effect measurements. While the thermal conductivity of the Ga-containing ABX_4 Zintls remains exceptionally low (<0.5 W m^{-1} K^{-1}, 350 °C), the variation in doping efficiency inspired us to consider alternate (hypothetical) compounds. To this end, we performed a computational survey over 27 ABX_4 compositions where A = (K, Rb, Cs), B = (Al, Ga, In), and X = (As, Sb, Bi). The predicted transport results are tabulated, and the thermoelectric potential is evaluated through use of the quality factor β.

METHODS

Experimental Section. Samples of $KAlSb_4$, $KGaSb_4$, $RbAlSb_4$, $RbGaSb_4$, $CsAlSb_4$, and $CsGaSb_4$ were synthesized from elemental reagents: K (ingot, Alfa 99.8%), Rb (ingot, Alfa 99.75%), Cs (liquid, Alfa 99.98%), Al (shot, Alfa 99.999%), Ga (liquid, Alfa 99.99%), and Sb (shot, Alfa 99.999%). Due to the reactivity of alkali metal precursors, all sample preparation was performed in a nitrogen glovebox (oxygen <3 ppm, water <1 ppm). Elemental reagents were sealed into tungsten carbide vials and ball milled for 90 min in a Spex 8000D high-energy ball mill. Note that an additional 5% excess alkali metal was added to each synthesis (e.g., $K_{1.05}GaSb_4$). Synthesis of Ba-doped samples followed an identical procedure, except for the addition of 2.5% Ba (ingot, Alfa 99.8%) before milling. Note that, to maintain doping stoichiometry *and* excess alkali content, doped samples were synthesized according to $(Ba_{0.025}K_{0.975})_{1.05}GaSb_4$.

For structure determination, we sealed undoped, as-milled powders into fused silica ampules and annealed them at 550 °C for 48 h under vacuum. Resulting powders were ground in an agate mortar and passed through a 50 μm mesh. We diluted all samples with amorphous silica powder at a molar ratio of 1:6 powder/silica to reduce X-ray absorption. Diluted powders were sealed within polyimide (Kapton) capillaries and measured at the Advanced Photon Source (APS) beamline 11-BM. Structure solution was performed using charge flipping and Rietveld refinement on the powder diffraction data within the Topas V6 software package.[51−54] Structures were cross-referenced with the published results on $KGaSb_4$ and $KAlSb_4$ as reported by Cordier and Ochmann.[49,50]

For transport measurements, as-milled (doped) powders were densified through reactive hot-pressing in a high-density graphite die under dynamic vacuum. Prior to use, the graphite die, plungers, and graphite foil liners were baked at 600 °C for a minimum of 30 min under dynamic vacuum. We loaded approximately 1.75 g of milled powder into the cooled die and transferred this to the hot press chamber. The chamber was evacuated to <5 mTorr and purged with argon to ∼0.75 atm thrice before the chamber was evacuated to <1 mTorr. A pressure of 25 MPa was applied to achieve a rough green body density before beginning the temperature profile. The sample was densified at 550 °C under 15 MPa of pressure for 12 h and then cooled to room temperature at a controlled rate of 100 °C/h. Note that this synthesis closely follows the methods outlined in our prior paper on $KGaSb_4$.[46] Hall effect measurements were performed in the Van der Pauw geometry on a custom built apparatus with a source current of 100 mA and a magnetic field of 2 T.

Thermal diffusivity measurements were made using a Netzsch laser flash apparatus (LFA) 457. The resulting diffusivity data were fit using a Cowen plus pulse correction numerical model. Samples were coated in a layer of graphite spray prior to measurement in order to reduce errors caused by sample emissivity. The total thermal conductivity of the alloyed samples was calculated using $\kappa = D\rho C_p$, where D is the thermal diffusivity, ρ is the mass density, and C_p is the volumetric heat capacity. The heat capacity was estimated using the Dulong−Petit approximation.

Computational. Thermoelectric properties of the ABX_4 family of Zintl phases were examined for 27 compounds, where A = (K, Rb, Cs), B = (Al, Ga, In), and X = (As, Sb, Bi). Hypothetical structures were constructed using $KAlSb_4$ as the prototype structure and were subsequently relaxed using density functional theory (DFT) and the plane-wave VASP software code.[55] The generalized gradient approximation (GGA) in the Perdew−Burke−Ernzerhof (PBE)[56] functional form was used within the projector augmented wave (PAW) formalism.[55] For structural relaxations, a procedure similar to that used in refs 46 and 47 was applied, with a plane-wave energy cutoff energy of 340 eV. We used nonspin polarized calculations, as all elements considered here are nonmagnetic.

To gauge the potential for thermoelectric performance, we employed the quality factor β, which provides a measure of zT, as presented in our prior publication.[57]

$$\beta \propto \frac{\mu_0 m_{\mathrm{DOS}}^{*\,3/2}}{\kappa_l} T^{5/2} \tag{1}$$

Here, T is the temperature, μ_0 the intrinsic charge carrier mobility, m^*_{DOS} the density-of-states (DOS) effective mass, and κ_l the lattice thermal conductivity. To evaluate μ_0 and κ_l, we utilized semiempirical models developed by combining physics-informed models with experimentally measured transport data.[57] The semiempirical model for μ_0 is motivated by the relationships describing electron−phonon scattering in band conductors, and given by $\mu_0 = A_0(B)^s(m_b^*)^{-t}$, where B is the bulk modulus, m_b^* is band effective mass, and A_0, s, and t are fitted parameters. Details of the semiempirical model for κ_l can be found in ref 58.

Electronic structures were calculated on a dense k-point grid with a fixed number of k-points. The k-point density is equivalent to a 16 × 16 × 16 k-point grid for diamond-Si and provides sufficiently converged electronic structure parameters. The parabolic band approximation was used to calculate m^*_{DOS}, such that the parabolic band contained the same number of states as the calculated DOS within a 100 meV energy window from the relevant band edges. The band effective mass was determined from m^*_{DOS} and band degeneracy N_b by assuming spherical and symmetric carrier pockets and using the relationship $m_b^* = m^*_{DOS}N_b^{-2/3}$. The bulk modulus B was calculated by fitting the Birch−Murnaghan equation of state.

In accordance with experimental results, we selected the series $AGaSb_4$ (A = K, Rb, Cs) for further calculations, including assessment

https://dx.doi.org/10.1021/acsaem.0c00048
ACS Appl. Energy Mater. 2020, 3, 2182−2191

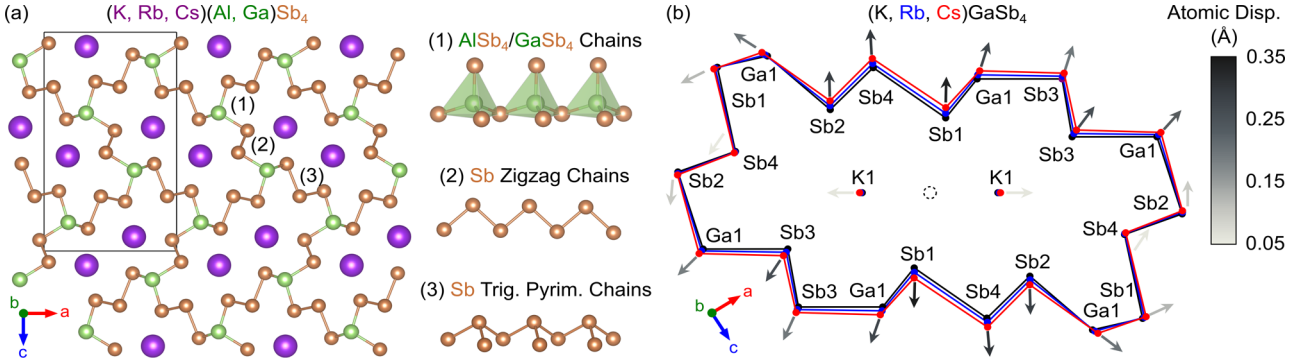

Figure 1. (a) ABX_4 class of Zintl phases consists of tunnel structures composed of an (Al, Ga)Sb_4 network that encapsulates a double tunnel of alkali metal (K, Rb, Cs) ions. The anionic network is composed of three distinct subunits that extend indefinitely into the *c*-direction: (1) corner-sharing (Al, Ga)Sb_4 tetrahedra, (2) Sb−Sb zigzag chains, and (3) trigonal pyramidal chains of Sb. (b) A schematic depiction of a single tunnel is shown to highlight structural changes with increasingly larger alkali metal cations. Atomic positions are shown to scale; direction of displacement is indicated by the arrow and magnitude by the shade. The vast majority of the structural changes occur in the *ac*-plane as shown, with *a* and *c* expanding roughly 1.7−2% while *b* expands only 0.2% between structures.

of phase stability and n-type dopability. The phase stability (against decomposition into competing phases) of $KGaSb_4$, $RbGaSb_4$, and $CsGaSb_4$ was assessed using the convex hull construction. Inspired by the fitted elemental-phase reference energies (FERE) approach,[59] the reference chemical potentials are obtained by fitting to a set of experimentally measured formation enthalpies. The fitted elemental-phase reference energies (μ^0) of elements K, Rb, Cs, Ga, and Sb are −1.135, −0.824, −0.957, −2.899, and −4.113 eV, respectively. For $KGaSb_4$, we considered KSb, K_3Sb, KSb_2, K_5Sb_4, GaSb, $KGaSb_2$, K_2GaSb_2, and $K_2Ga_2Sb_3$ as competing phases. For $RbGaSb_4$, RbSb, Rb_3Sb, $RbSb_2$, GaSb, and Rb_2GaSb_2 were considered. Calculations with $CsGaSb_4$ considered competition from GaSb, CsSb, Cs_2Sb, Cs_3Sb, Cs_5Sb_8, Cs_2GaSb_2, and Cs_6GaSb_3.

To understand the native defect chemistry of $AGaSb_4$ (A = K, Rb, Cs) and extrinsic doping of $RbGaSb_4$, we performed first-principles defect calculations using the VASP software package.[55] The GGA-PBE approximation was performed within the PAW formalism.[56,60] Total energies of defect supercells containing 192 atoms were calculated with a plane-wave cutoff of 340 eV and a Γ-centered Monkhorst pack *k*-point grid of 4 × 4 × 4. The defect supercells were relaxed following the procedure outlined in ref 59. The defect formation enthalpies ($\Delta H_{D,q}$) were calculated from the total energies as

$$\Delta H_{D,q}(E_F, \mu) = (E_{D,q} - E_H) + \sum_i n_i\mu_i + qE_F + E_{corr} \quad (2)$$

where $E_{D,q}$ and E_H are the total energies of the defect and host supercell, respectively. μ_i is the chemical potential of elemental species *i* added ($n_i < 0$) or removed ($n_i > 0$) from the host supercell to form the defect. E_F is the Fermi energy, and E_{corr} comprises all the finite-size corrections, within the supercell approach. The chemical potentials μ_i were expressed relative to the reference elemental phase such that $\mu_i = \mu_i^0 + \Delta\mu_i$, where μ_i^0 is the reference elemental chemical potential calculated using FERE[59] and $\Delta\mu_i$ is the deviation from the reference elemental phase. The bounds on $\Delta\mu_i$ were set by the region of phase stability, $\Delta\mu_i = 0$ corresponding to *i*-rich conditions.

The band gap underestimation within DFT-GGA was corrected by applying band edge shifts determined from GW quasiparticle energy calculations, as described in ref 61. The following corrections were included in E_{corr} following the methodology in ref 62: (1) image charge correction for charged defects, (2) potential alignment correction for charged defects, (3) band filling correction for shallow defects, and (4) band gap correction for shallow donors/acceptors. The calculations were set up and analyzed using a software package recently developed for automation of defect calculations.[63]

RESULTS AND DISCUSSION

Discovery and Structure of the ABX_4 Zintl Antimonides. The prototype structure $KAlSb_4$ and its isostructural analogue $KGaSb_4$ were originally reported by Cordier and Ochmann in the 1990s.[49,50] However, despite their efforts in analogous chemical spaces (e.g., discovery of Cs_2GaSb_2),[64] they never reported Rb- or Cs-containing analogues to $KAlSb_4$ or $KGaSb_4$. Here, we report the discovery of $RbAlSb_4$, $RbGaSb_4$, $CsAlSb_4$, and $CsGaSb_4$. These phases were initially identified from laboratory X-ray diffraction, although we performed follow-up measurements at the Advanced Photon Source (APS 11-BM) for confirmation. As internal references, we also included fresh samples of $KGaSb_4$ and $KAlSb_4$ in our experiments. Direct structure solution using charge flipping methods confirms that $RbAlSb_4$, $RbGaSb_4$, $CsAlSb_4$, and $CsGaSb_4$ crystallize in the $KAlSb_4$ structure type. All diffraction experiments, alongside the refined results, can be found in the SI, Figures S1−S6.

Figure 1a exhibits the crystal structure of the ABX_4 Zintl phases. The features are generally reminiscent of other tunnel-like Zintl materials (e.g., $BaGa_2Sb_2$,[35,48] $Ba_3Ga_4Sb_5$,[65] $Ba_4In_8Sb_{16}$[66]), although the AlSb/GaSb networks in the ABX_4 Zintls form double tunnels of alkali metal ions that extend in the *b*-direction. The tunnel walls are tiled in a herringbone-like pattern (*Pnma* space group) in the *ac*-plane. The AlSb/GaSb polyanionic framework contains four unique Sb sites and three unique types of Sb coordination. Extending as infinite chains into the page, we find (1) $AlSb_4/GaSb_4$ corner-sharing tetrahedra, (2) Sb−Sb zigzag chains, and (3) Sb−Sb trigonal pyramidal chains. As Zintl compounds generally maintain semiconducting charge balance, all Sb atoms in this structure contain lone pairs.

Figure 1b shows a isolated representation of the ABX_4 double tunnel structure. The colors indicate the structural changes as we transition between $KGaSb_4$ (black), $RbGaSb_4$ (blue), and $CsGaSb_4$ (red). The Al-series is qualitatively identical. Comparisons between the Al and Ga systems (e.g. $KAlSb_4$ and $KGaSb_4$) are significantly more subtle—an analogous figure can be found in the SI, Figure S7. The atomic positions derived from Rietveld analysis of synchrotron data were shifted such that the centers of mass for each tunnel (denoted by the dashed circle) coincide. The absolute changes in the atomic positions are shown to scale. The direction of the

https://dx.doi.org/10.1021/acsaem.0c00048
ACS Appl. Energy Mater. 2020, 3, 2182−2191

arrow indicates the direction of displacement, and the shade of the arrow indicates the magnitude.

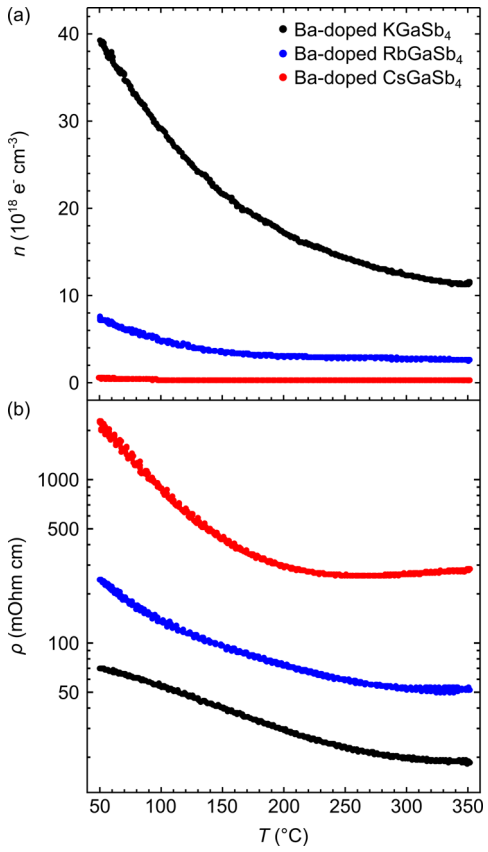

Figure 2. (a) Hall effect measurements on 2.5% Ba-doped samples of $KGaSb_4$, $RbGaSb_4$, and $CsGaSb_4$ reveal that all materials are n-type dopable with Ba. However, the doping efficiency of Ba falls off dramatically as we transition from $KGaSb_4$ (1.1×10^{19} e^- cm^{-3}, 350 °C), to $RbGaSb_4$ (2.7×10^{18} e^- cm^{-3}, 350 °C), to $CsGaSb_4$ (3.0×10^{17} e^- cm^{-3}, 350 °C). (b) Electrical resistivity measurements track changes in the Hall carrier concentration. However, resistivity also shows temperature-activated behavior independent of the carrier concentration, presumed to be caused by oxidation at grain boundaries.

The most dramatic changes are observed in the Sb and Al/Ga atoms which most closely coordinate the alkali metal tunnels. Geometrically, this causes a significant increase in the cross-sectional area of the tunnel structure. In fact, expansion within the *ac*-directions (cross-sectional) far outstrips that of the *b*-direction (along tunnel). From $KGaSb_4$ (774.06 Å^3, a = 10.347 Å, b = 4.201 Å, c = 17.807 Å) to $RbGaSb_4$ (808.15 Å^3, a = 10.525 Å, b = 4.210 Å, c = 18.104 Å), the *a*- and *c*-directions expand approximately 1.7% whereas the *b*-direction expands only by 0.2%. Similarly, for the transition between $RbGaSb_4$ and $CsGaSb_4$ (836.07 Å^3, a = 10.742 Å, b = 4.219 Å, c = 18.448 Å), the *a*-direction expands 2.1%; *c* expands 1.9%, and *b* expands only 0.2%. The cell volume increases monotonically with increasing alkali metal size and decreases when Ga is substituted for Al. These observations are consistent with the increasing ionic radii of the alkali metals (K, Rb, Cs) and the decreasing covalent radii of the group 13 metals (Al, Ga).

At room temperature, the thermal parameters for the alkali metal ions seem typical for related Zintl phases. For all ABX_4 Zintls studied here, the isotropic thermal parameter (B_{eq}) ranges between 1.7 and 1.9 Å^2. This appears to be consistent with related compounds. Consider $KGaSb_4$ (B_{eq} ~ 1.9 Å^2) compared to the chemically related compounds $KGaSb_2$ (B_{eq} ~ 2.7−3.7 Å^2), K_2GaSb_3 (B_{eq} ~ 2.2−3.1 Å^2), and K_2GaSb_2 (B_{eq} ~ 1.8−2.5 Å^2).[67−69] These values are also comparable to the B_{eq} of K-containing type-II clathrates (e.g., $K_2Ba_{14}Ga_{30}Sn_{106}$, B_{eq} ~ 1.5 Å^2).[70] It is important to keep in mind, however, that these measurements were performed on powders. Furthermore, the structure is clearly anisotropic, and the isotropic thermal parameters may not adequately describe complex Zintl phases.

Due to the high resolution of APS 11-BM, we resolved a slight anomaly which is not observable by laboratory X-ray diffraction. Many peaks display slight asymmetry or shoulder peaks which cannot be modeled by microstructural or fundamental parameter peak shapes. The pattern appears as though two slightly different lattice parameters are present for a single compound. An exhaustive search for a new space group or crystal system yielded no results that outperform the original prototype. Changes in processing had a minimal effect on the anomaly, and the effect persisted between batches synthesized independently. Calibration standards from APS confirm no beamline issues, and reflections cannot be ascribed to impurities. We suspect that ABX_4 powders are more reactive than they initially appear. While samples were synthesized entirely under nitrogen, transport to APS was performed in sealed Kapton capillaries. Spurious oxidation of samples would vary depending on Kapton permeability and seal quality. For this data set, $KAlSb_4$, $KGaSb_4$, $RbAlSb_4$, $CsAlSb_4$, and $CsGaSb_4$ show a minimal effect and need no special attention. $RbGaSb_4$ shows significant peak asymmetry and requires additional fitting; details can be found alongside Figure S4. The anomaly does not affect the conclusions derived from the diffraction data and would not be resolved outside of synchrotron sources. Considering that $KAlSb_4$ and $KGaSb_4$ showed potential as n-type Zintl thermoelectrics, the next natural step is to dope the new ABX_4 materials and determine their amenability to n-type doping.

Experimental Doping of ABX_4 Zintls with Ba. Both $KAlSb_4$ and $KGaSb_4$ were dopable to approximately 2×10^{19} e^- cm^{-3} with Ba. Solid solutions with Ba were noted up to approximately 2% substitution on the alkali site (e.g., $K_{0.98}Ba_{0.02}GaSb_4$). Monotonic changes in the electronic properties (Seebeck coefficient, electrical resistivity, Hall effect) were observed, confirming successful doping.[46,47] Both materials showed good thermoelectric performance, nearing zT ~ 1 at 400 °C with minimal optimization. For this paper, we have opted to restrict the scope of additional experiments to the Ga-based compounds, as they tend to outperform the Al-based materials. However, we expect the results to generalize to the Al-based compounds.

All undoped ABX_4 Zintls present as intrinsic semiconductors with high electrical resistivity, low carrier concentration, and bipolar Seebeck coefficients. To assess the n-type dopability of the new ABX_4 materials, we doped $RbGaSb_4$ and $CsGaSb_4$ with 2.5% Ba. A fresh sample of Ba-doped $KGaSb_4$ was also included as an internal reference sample. At these concentrations, we see evidence of a Ba-rich impurity phase, indicating saturation of the Ba solubility in the ABX_4 phase. Figure 2 shows the temperature-dependent Hall carrier concentration and electrical resistivity for Ba-doped $KGaSb_4$, $RbGaSb_4$, and $CsGaSb_4$. Measurements shown include both heating and cooling data.

https://dx.doi.org/10.1021/acsaem.0c00048
ACS Appl. Energy Mater. 2020, 3, 2182−2191

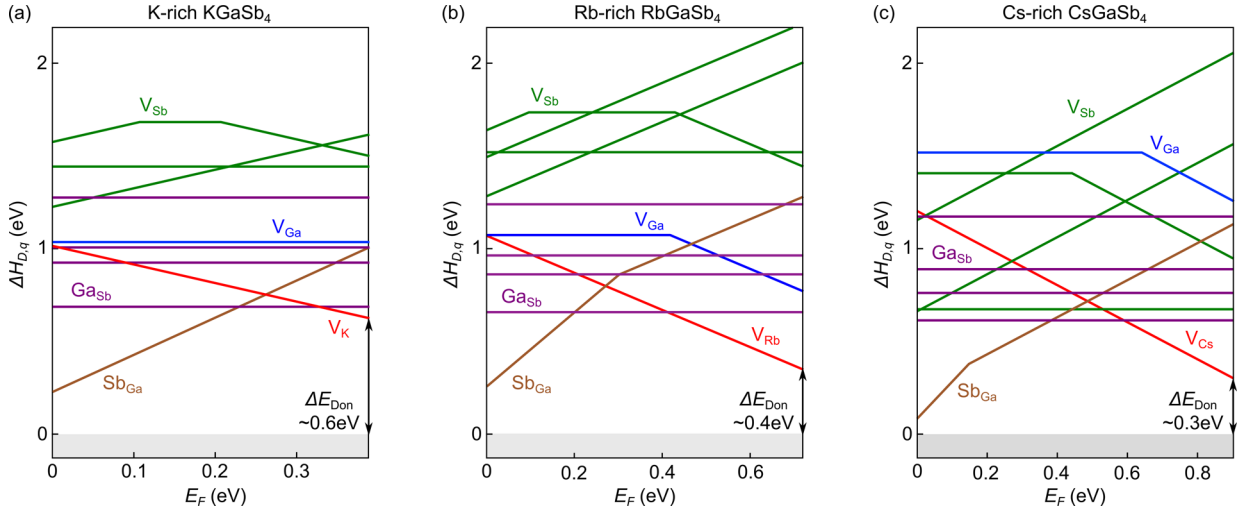

Figure 3. Native defect formation enthalpies ($\Delta H_{D,q}$) are shown as a function of the Fermi level (E_F) for (a) K-rich $KGaSb_4$, (b) Rb-rich $RbGaSb_4$, and (c) Cs-rich $CsGaSb_4$. Alkali metal vacancies (red lines) are the lowest-energy acceptor defects while antisite Sb_{Ga} defects (brown lines) are the lowest-energy donor defects. E_F is referenced to the valence band maximum such that E_F values range from 0 to the band gap energy E_g. Multiple lines of the same color represent the same defect type at different crystallographic sites. The relatively high formation energy of acceptor cation vacancies facilitates extrinsic n-type doping. ΔE_{Don} represents the energy window for extrinsic n-type doping.

Our previous results on Ba-doped $KGaSb_4$ found that the Hall carrier concentration saturates at approximately 2.1×10^{19} e^- cm^{-3} at 400 °C. This agrees well with the present study, where Ba-doped $KGaSb_4$ saturates near 1.1×10^{19} e^- cm^{-3} at 350 °C. The reduced temperatures in this work are to avoid sublimation of $RbGaSb_4$ and $CsGaSb_4$ at high temperatures. The qualitative trend for $KGaSb_4$ also tracks our previous publication well, showing a Hall carrier concentration that *decreases* with temperature. We do not observe any hysteresis during thermal cycling of the ABX_4 samples below 350 °C, so we do not suspect permanent loss of the alkali metal as a contributing factor to the decreasing carrier concentration. Instead, this observation may be explained by the thermal activation of compensating defects (e.g., alkali metal vacancies), nonparabolicity of the bands, or energy-dependent electron scattering rates that evolve with temperature.

The electronic resistivity exhibits two effects: (1) increasing resistivity due to decreased doping efficiency moving from $KGaSb_4$, $RbGaSb_4$, to $CsGaSb_4$, and (2) decreasing resistivity with temperature. The general changes in the order of magnitude of the resistivity trend sensibly with changes in doping efficiency of Ba. However, the decreasing resistivity with temperature requires some explanation. As noted in previous publications, many Zintl phases show high room-temperature resistivity. The thermally activated behavior is often attributed to oxidation at grain boundaries and has been observed in Ca_3AlSb_3, Sr_3AlSb_3, Sr_3GaSb_3, and $KAlSb_4$.[31−34,47] We have shown that intensive refinement of processing procedures can reduce the effect, although it is difficult to fully eliminate it.[46] This is consistent with our hypothesis regarding the potential compositional inhomogeneity in X-ray results.

While $RbGaSb_4$ and $CsGaSb_4$ are successfully doped n-type with substitution of Ba, the doping efficiency is significantly reduced when compared to $KGaSb_4$. At 350 °C, $RbGaSb_4$ has $n \sim 2.7 \times 10^{18}$ e^-cm^{-3}, while $CsGaSb_4$ is reduced to $n \sim 3.0 \times 10^{17}$ e^- cm^{-3}. The strong changes in the carrier concentration contrast the relatively small structural changes and suggest that a more in-depth investigation into the underlying defect energetics is required.

Defect Chemistry of ABX_4 Zintl Phases. To provide insight into the n-type dopability of $KGaSb_4$, $RbGaSb_4$, and $CsGaSb_4$, we turn to first-principles defect calculations. Focusing on the native defects, Figure 3a−c summarizes the calculated defect formation enthalpies. For consistency, all calculations were performed under alkali-rich conditions. While the alkali metal chemical potential is maximized, the formation of alkali vacancies is suppressed, which is conducive for minimizing compensation and maximizing extrinsic n-type doping. However, we note that the single-phase regions for the ABX_4 phases are relatively narrow, suggesting that the specific choice of chemical potentials has only a minor effect.

In Figure 3a−c, the defect formation enthalpy ($\Delta H_{D,q}$) is calculated as a function of the Fermi energy (E_F), which is referenced to the valence band maximum and ranges from 0 to the band gap energy (E_g). For the defect calculations, the band gaps were calculated with a higher-accuracy many-body GW-based methods (see Methods section). The equilibrium Fermi energy can be calculated by self-consistently solving for charge neutrality between the charged defects and free carriers. To the first order, the equilibrium Fermi energy lies near the intersection of the lowest-energy acceptors and donors. In all three systems, the lowest-charged defects are the alkali metal vacancies $V_{K,Rb,Cs}$ (red) and the Sb_{Ga} (brown) antisite donor defect. In each of the three Zintl phases ($KGaSb_4$, $RbGaSb_4$, $CsGaSb_4$), we find that the equilibrium Fermi energy lies roughly in the middle of the gap, which is consistent with the observed intrinsic nature of the undoped phases.

The dopability of a semiconductor is quantified by the achievable carrier type(s) and concentrations. It depends on several factors, including (1) the formation energetics of native defects, and (2) the existence of dopants with sufficient solubility and desired electronic properties. The former depends on the formation energy of the lowest-energy native acceptor and donor defects. Materials with low formation energy acceptors (e.g., alkali vacancies) are difficult to dope n-type due to defect compensation. In this context, n-type

https://dx.doi.org/10.1021/acsaem.0c00048
ACS Appl. Energy Mater. 2020, 3, 2182−2191

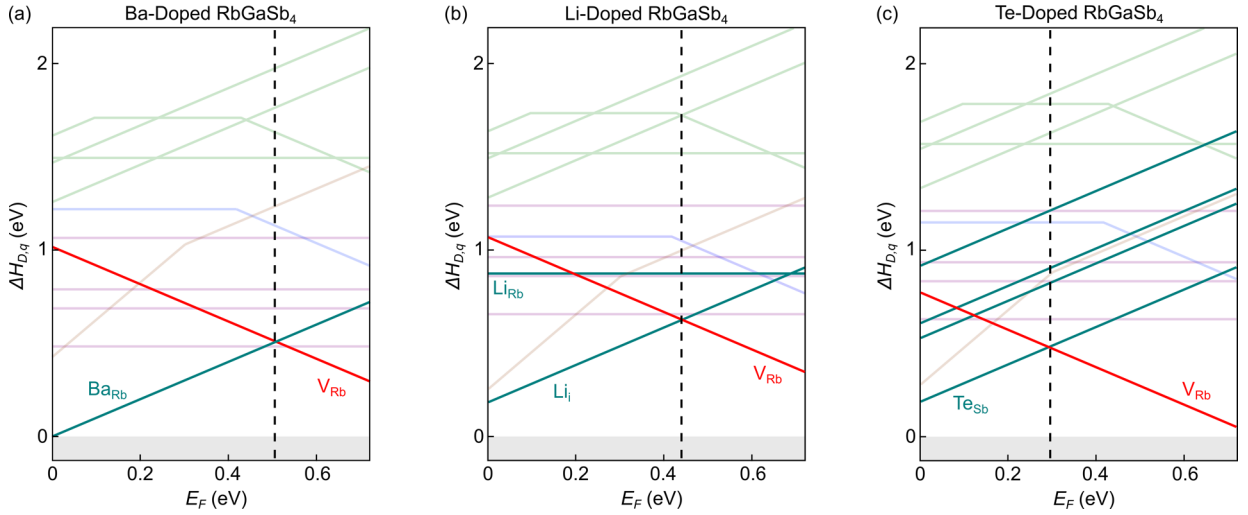

Figure 4. Extrinsic doping of $RbGaSb_4$ used as a demonstration of extrinsic doping in the ABX_4 compounds. Formation enthalpies ($\Delta H_{D,q}$) are calculated under conditions that maximize the chemical potential (and solubility) of the dopant species. The vertical dashed line shows the equilibrium Fermi energy at 823 K (growth temperature of $RbGaSb_4$). (a) Consistent with experiment, Ba-doped $RbGaSb_4$ should be n-type. (b) Lithium should also behave as a weak n-type dopant, although the effectiveness is decreased in comparison to Ba. (c) The influence of Te-doping highlights some interesting secondary effects; while Te_{Sb} defects are low-energy, calculating the diagram in the Te-rich regime dramatically changes V_{Rb} compensation.

dopability can be gauged from the energy "window" created at the conduction band minimum by the lowest-energy native acceptor defect. In Figure 3a–c, the n-type dopability window is denoted by ΔE_{Don}.

In Figure 3, $KGaSb_4$ has the largest ΔE_{Don} (~0.6 eV), followed by $RbGaSb_4$ (~0.4 eV) and $CsGaSb_4$ (~0.3 eV). The reduced ΔE_{Don} in $CsGaSb_4$ can be partly attributed to the widened band gap (compared to $KGaSb_4$) and the associated lowering of the cation vacancy formation energy. Thus, while $RbGaSb_4$ and $CsGaSb_4$ are still n-type dopable, they are probably *less dopable* when compared to $KGaSb_4$. As referenced before, however, the ultimate dopability also depends on finding a suitable low-energy dopant that has sufficient solubility. To examine the action of some intuitive dopants in the ABX_4 phases, let us specifically consider extrinsic doping of $RbGaSb_4$.

For $RbGaSb_4$, we computationally assessed three plausible n-type dopants: Ba_{Rb}, Li_i, and Te_{Sb}. For completeness, we consider all possible substitutions in our calculations (e.g., Ba could substitute as Ba_{Rb}, Ba_{Ga}, or Ba_{Sb}). In the case of interstitial Li, the position of the Li interstitial is determined using a Voronoi tessellation scheme as implemented in the pylada-defects software.[63] The resulting defect energetics for Ba-doping, Li-doping, and Te-doping are shown in Figure 4a–c, respectively. For each case, the chemical potential conditions are chosen to maximize the chemical potential of the dopant (subsequently maximizing dopant solubility) while maintaining phase stability of $RbGaSb_4$. Note that when considering an extrinsic dopant, the phase stability region of $RbGaSb_4$ must be recalculated in the Rb–Ga–Sb-dopant phase space. Any additional competing phases that involve the dopant species must be considered in re-establishing the single-phase region of $RbGaSb_4$.

For Ba-doping (Figure 4a), Ba_{Rb} is the most favorable dopant defect, as expected. The equilibrium Fermi energy calculated at 550 °C (growth temperature) is shown with a dashed vertical line, which lies close to the intersection of the lowest-energy acceptor (V_{Rb}) and donor (Ba_{Rb}). Since the Fermi energy is set closer to the conduction band, Ba-doped $RbGaSb_4$ is predicted to be doped n-type, in agreement with experiment. Although less favorable than Ba_{Rb}, lithium (Figure 4b) should lightly dope $RbGaSb_4$ n-type. However, the practical doping efficiency in Li-doped $RbGaSb_4$ may suffer due to the relatively low energy of Li_{Rb} neutral defects. The case of Te-doping (Figure 4c) is perhaps the most interesting case. Here, despite substitutional Te_{Sb} being a favorable n-type defect (resembling the case of Li_i), the Fermi energy has been pushed into the lightly doped p-type regime. As an anion, maximizing the Te chemical potential ultimately pushes the system into a cation-poor regime. As a consequence, compensation by rubidium vacancies is sharply increased, and the material becomes p-type. We also note that the formation enthalpy of Te_{Sb} shows strong site dependence, increasing as we transition from Te_{Sb1}, Te_{Sb2}, Te_{Sb3}, and Te_{Sb4}.

Our calculations support that (1) undoped $RbGaSb_4$ and $CsGaSb_4$ are intrinsic, and (2) $RbGaSb_4$ and $CsGaSb_4$ can be extrinsically doped n-type. These results are in excellent agreement with experiments. More importantly, the calculations have revealed the reason for the strong changes in carrier concentration among $KGaSb_4$, $RbGaSb_4$, and $CsGaSb_4$. It is unlikely that Ba-doping alone will achieve the degenerate n-type doping that is needed to optimize the thermoelectric performance in $RbGaSb_4$ or $CsGaSb_4$. Future studies will consider a more exhaustive set of n-type dopants for $RbGaSb_4$ and $CsGaSb_4$. For example, rare-earth metals, interstitial dopants, and Ga-site dopants are several unexplored possibilities.

Experimental Thermal Properties of ABX_4 Zintls. The defect energetics and Ba-doping effectiveness in $KGaSb_4$, $RbGaSb_4$, and $CsGaSb_4$ showed a strong dependence on the alkali metal cation despite minor changes in the crystal structure. The addition of heavier cations could be reasonably expected to have a strong influence on the thermal conductivity as well. Generally, the Zintl phases tend to have *intrinsically* low lattice thermal conductivity owing to their complex structures, soft bonding, and heavy elements.[2,3]

https://dx.doi.org/10.1021/acsaem.0c00048
ACS Appl. Energy Mater. 2020, 3, 2182–2191

However, the defect energetics and dopability of $KGaSb_4$, $RbGaSb_4$, and $CsGaSb_4$ showed a strong dependence on the alkali metal cation despite relatively minor changes in the crystal structure. The addition of heavier cations could be reasonably expected to have a strong influence on the thermal conductivity as well. Here we present a brief comparison of the thermal properties of the Ga-based ABX_4 Zintls.

To reduce the effect of bipolar contributions, we elected to measure the thermal properties of the Ba-doped samples. Polycrystalline pellets of $KGaSb_4$, $RbGaSb_4$, and $CsGaSb_4$ were measured up to 350 °C on both heating and cooling. Sample densities are consistently >97% of the theoretical densities predicted by X-ray diffraction. The total thermal conductivity is included in the Supporting Information, Figure S8. To separate the electronic contribution, the Wiedemann–Franz law ($\kappa_e = LT/\rho$) was used to calculate the lattice thermal conductivity ($\kappa_l = \kappa - \kappa_e$). In our previous work, we used the high-temperature Seebeck coefficient data to explicitly calculate the Lorenz number L at each temperature. However, Seebeck measurements are unreliable for $RbGaSb_4$ and $CsGaSb_4$ due to the relatively low carrier concentrations. As such, the Lorenz number was approximated as 2.44×10^{-8} W Ω K^{-2}. Regardless, the high resistivity of $RbGaSb_4$ and $CsGaSb_4$ renders the electronic contribution fairly insignificant. Figure 5 demonstrates the resulting lattice thermal conductivity for $KGaSb_4$, $RbGaSb_4$, and $CsGaSb_4$.

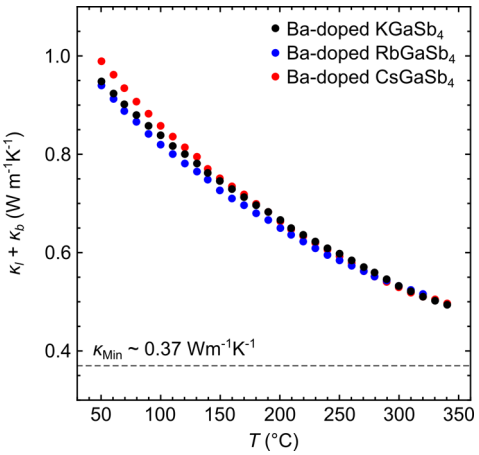

Figure 5. Lattice thermal conductivity values for Ba-doped samples of $KGaSb_4$, $RbGaSb_4$, and $CsGaSb_4$ are exceptionally low. By 350 °C, all materials are below 0.5 W m^{-1} K^{-1} and are quickly nearing the glassy limit approximated by the Debye–Callaway model. The similarity between the compounds is striking, considering the significant difference in mass between K and Cs. There may be a small portion of the high-temperature lattice thermal conductivity that includes a bipolar component due to the modest n-type doping of the Rb and Cs compounds.

All three materials possess extraordinarily low lattice thermal conductivity, reaching <0.5 W m^{-1} K^{-1} by 350 °C. These values are not far from the optical phonon dominated "glassy limit" (κ_{Min}) as approximated by the Debye–Callaway model. For $KGaSb_4$, the theoretical minimum is approximately $\kappa_{Min} \sim$ 0.37 W m^{-1} K^{-1} (gray dashed line). Perhaps the more surprising conclusion is the *similarity* among the three materials, which are functionally identical within error. We suspect that the Sb-framework must drive the majority of the thermal transport; the acoustic branches in particular should have strong Sb-character due to Sb's heavy mass. This is reflected in the minimal impact of $KGaSb_4$–$KAlSb_4$ alloying in our prior work.[46] Likewise, it appears that the choice of alkali metal has a limited role in the thermal conductivity. It would be interesting, however, to alloy with significantly smaller ions. For example, incorporation of Li (as suggested in the defect calculations) may be able to contribute as a surrogate "rattler" within the tunnel structures, analogous to the effects observed in the clathrates.

Predicted TE Performance of ABX_4 Zintl Phases. Our previous studies revealed that $KAlSb_4$ and $KGaSb_4$ are excellent candidates for thermoelectrics due to their extremely low lattice thermal conductivity and high electron mobility.[46,47] The new additions to the ABX_4 family, $RbAlSb_4$, $RbGaSb_4$, $CsAlSb_4$, and $CsGaSb_4$, also show potential. However, we have also shown that the critical parameter, the dopability, can change dramatically with choice of the alkali metal cation. To this end, exploring other reasonable ABX_4 combinations (particularly those with smaller band gaps) would be valuable. To this end, we evaluated 21 hypothetical ABX_4 compounds along with the 6 experimentally realized phases using DFT calculations. In total, 27 ABX_4 phases were evaluated, corresponding to all combinations of A = (K, Rb, Cs), B = (Al, Ga, In), and X = (As, Sb, Bi). All 27 phases retain the prototype ABX_4 structure upon DFT relaxation. Of the 27 compounds, 21 exhibit nonzero DFT (GGA-PBE) band gaps; for these phases, we assess their n- and p-type thermoelectric performance with the thermoelectric quality factor β (see Methods section). The results for these 21 compounds are presented in Table 1.

The compounds in Table 1 are sorted in the descending order of their β_n values. For reference, β_n and β_p values of PbTe are ~15. As discussed in prior studies,[47,57] β is a measure of the potential for thermoelectric performance, assuming that the material can be appropriately doped to optimize TE performance. All 21 compounds in Table 1 exhibit relatively high β_n values, suggesting that the family of ABX_4 Zintl phases are particularly interesting as n-type thermoelectric materials. For all 21 compounds, β_n is larger than β_p. This observation is consistent with the conclusions of our previous study[47] where we found that Zintl phases are generally promising n-type TE materials, despite their experimental proclivity for p-type doping. Since κ_l is the same for both β_n and β_p, the higher values of β_n directly stem from high electron mobilities (μ_n). In general, the electron mobilities are more than an order of magnitude higher than hole mobilities.

The observed difficulty in n-type doping of ABX_4 phases with larger band gaps (e.g., $CsGaSb_4$ vs $KGaSb_4$) suggests that smaller band gap compounds may be of interest. Additionally, the Bi- and In-containing ABX_4 Zintl phases exhibit particularly high β_n values (Table 1). We performed an round of exploratory syntheses to investigate additional compositions. Initial attempts at synthesizing $CsGaBi_4$, $KInSb_4$, and $KGaBi_4$ were unsuccessful. Stoichiometric mixtures of K + In + Sb_4 form the corresponding 2–2–3 structure and pnictogen (e.g., $2K + 2In + 8Sb \rightarrow K_2In_2Sb_3 + 5Sb$). However, the presence of the 2–2–3 structure is not necessarily at odds with formation of the 1–1–4 structure, as the K–Ga–Sb system also shows a corresponding 2–2–3. For both bismides, stoichiometric mixtures decompose even further, lacking any nearby ternary compounds (e.g., $K + Ga + 4Bi \rightarrow KBi_2 + Ga + 2Bi$). Further studies are required to

https://dx.doi.org/10.1021/acsaem.0c00048
ACS Appl. Energy Mater. 2020, 3, 2182–2191

Table 1. Hypothetical ABX_4 Zintl Phases Where A = (K, Rb, Cs), B = (Al, Ga, In), and X = (As, Sb, Bi), Created by Chemical Substitution in the $KAlSb_4$ Prototype Structure[a]

compd	β_n	β_p	E_g (eV)	$m^*_{b,CB}$ (m_e)	$m^*_{b,VB}$ (m_e)	μ_n (cm^2/(V s))	μ_p (cm^2/(V s))	κ_l (W/mK)
$KAlBi_4$	39.2	25.1	0.01	0.081	0.17	97.6	32.1	0.78
$CsAlBi_4$	32.5	3.5	0.07	0.112	0.75	55.8	3.2	0.72
$KInBi_4$	31.5	16.4	0.04	0.115	0.80	51.5	2.8	0.70
$CsInSb_4$	25.8	15.6	0.25	0.087	0.64	137.3	6.9	1.19
$CsGaSb_4$	25.8	8.2	0.31	0.073	0.50	122.4	6.9	0.90
$RbInSb_4$	24.7	16.7	0.22	0.085	0.51	141.4	9.5	1.24
$KInSb_4$	24.3	22.4	0.20	0.085	0.45	146.0	12.0	1.31
$RbAlBi_4$	23.6	6.0	0.08	0.099	0.98	72.2	2.3	0.77
$RbGaSb_4$	23.4	17.5	0.30	0.077	0.25	115.1	20.4	0.98
$CsAlSb_4$	23.4	12.3	0.32	0.083	0.48	103.5	7.5	0.94
$KGaSb_4$	22.9	5.0	0.25	0.076	0.30	119.8	15.2	1.03
$RbGaAs_4$	22.7	14.9	0.23	0.087	0.56	133.5	8.3	1.31
$RbAlSb_4$	21.4	4.7	0.26	0.086	0.33	99.4	13.0	1.02
$KGaAs_4$	21.0	12.3	0.22	0.088	0.42	134.7	12.9	1.43
$KAlSb_4$	20.7	5.3	0.21	0.085	0.26	103.4	19.9	1.09
$RbAlAs_4$	19.6	14.5	0.21	0.094	0.49	120.1	10.1	1.46
$KAlAs_4$	17.8	3.5	0.16	0.097	0.46	116.5	11.3	1.59
$CsInAs_4$	15.4	11.7	<0.01	0.322	0.51	16.6	8.4	1.17
$RbInAs_4$	12.8	12.0	<0.01	0.393	0.44	12.5	10.8	1.27
$CsGaAs_4$	9.6	3.2	0.17	0.127	0.80	74.7	4.8	1.22
$CsAlAs_4$	9.6	7.0	0.17	0.118	0.63	85.0	6.9	1.30

[a]Predicted n- and p-type thermoelectric quality factor (β) is calculated for phases with non-zero DFT (GGA-PBE) band gap. Calculated transport parameters: band effective mass (m^*_b), room-temperature carrier mobility (μ), and room-temperature lattice thermal conductivity (κ_l) are shown for each compound. Compounds in bold denote phases that have been experimentally realized in this study. For reference, β_n and β_p values of PbTe are ~15.

exhaustively search the potential chemical space of the ABX_4 Zintl phases; arsenides may be a natural starting point.

CONCLUSION

In this work, we reported the discovery of four new ABX_4 Zintl phases: $RbAlSb_4$, $RbGaSb_4$, $CsAlSb_4$, and $CsGaSb_4$. All four new phases are structural analogues of $KAlSb_4$ and $KGaSb_4$, previously demonstrated as promising n-type thermoelectric materials (zT ~ 1, 350−400 °C). We examined structural trends in the ABX_4 family of Zintl materials, highlighting the influence of the alkali metal cation (K, Rb, Cs) on the structure. Our experimental work focused primarily on the Ga-containing antimonides, drawing comparisons between the K-, Rb-, and Cs-containing analogues. We have demonstrated n-type doping of $RbGaSb_4$ and $CsGaSb_4$ with Ba, although the Hall carrier concentrations achieved in these phases are significantly lower than in $KGaSb_4$. First-principles defect calculations provided critical insight into the reduced efficacy of Ba in $RbGaSb_4$ and $CsGaSb_4$. As we consider heavier alkali metal cations, the associated alkali metal vacancies become progressively more favorable and hinder n-type doping. However, all materials possess a sizable "dopability window" and should be amenable to extrinsic dopants. Consequently, we also investigated the influence of extrinsic dopants on the defect energetics, examining the effect of Ba, Li, and Te on $RbGaSb_4$. As expected of a complex Zintl phase, thermal transport remains excellent, falling below <0.5 W m^{-1} K^{-1} by 350 °C in $RbGaSb_4$ and $CsGaSb_4$. Considering the strong influence of chemistry on the dopability, we also performed a computational survey of 27 ABX_4 compositions where A = (K, Rb, Cs), B = (Al, Ga, In), and X = (As, Sb, Bi), assessing their transport properties and TE potential. Ultimately, our work has demonstrated the experimental realization of four new materials, demonstrated their potential as n-type TE materials, and tripled the number of known compounds in the ABX_4 family of Zintl phases.

ASSOCIATED CONTENT

Supporting Information

The Supporting Information is available free of charge at https://pubs.acs.org/doi/10.1021/acsaem.0c00048.

Additional diffraction, structural, and transport data (PDF)

AUTHOR INFORMATION

Corresponding Authors

Brenden R. Ortiz − *Colorado School of Mines, Golden, Colorado 80401-1887, United States; University of California Santa Barbara, Santa Barbara, California 93106-9010, United States;* orcid.org/0000-0002-1333-7003; Email: ortiz.brendenr@gmail.com

Eric S. Toberer − *Colorado School of Mines, Golden, Colorado 80401-1887, United States*; Email: etoberer@mines.edu

Authors

Prashun Gorai − *Colorado School of Mines, Golden, Colorado 80401-1887, United States;* orcid.org/0000-0001-7866-0672

Tara Braden − *Colorado School of Mines, Golden, Colorado 80401-1887, United States*

Erik A. Bensen − *Colorado School of Mines, Golden, Colorado 80401-1887, United States*

Stephen D. Wilson − *University of California Santa Barbara, Santa Barbara, California 93106-9010, United States*

Vladan Stevanović − *Colorado School of Mines, Golden, Colorado 80401-1887, United States*

https://dx.doi.org/10.1021/acsaem.0c00048
ACS Appl. Energy Mater. 2020, 3, 2182−2191

Complete contact information is available at:
https://pubs.acs.org/10.1021/acsaem.0c00048

Notes

The authors declare no competing financial interest.

■ ACKNOWLEDGMENTS

B.R.O., P.G., V.S, and E.S.T. acknowledge support from National Science Foundation Grant 1729594. This work was supported by the NASA Science Missions Directorate's Radioisotope Power Systems Thermoelectric Technology Development Project. B.R.O. also acknowledges support from the California NanoSystems Institute through the Elings Fellowship program. S.D.W. acknowledges support from 538 DOE, Office of Science, Basic Energy Sciences, under Award DE-SC0017752. S.D.W. also acknowledges support from the UC Santa Barbara NSF Quantum Foundry funded via the Q-AMASE-i initiative under award DMR-1906325. Use of the Advanced Photon Source at Argonne National Laboratory was supported by the U.S. Department of Energy, Office of Science, Office of Basic Energy Sciences, under Contract DE-AC02-06CH11357. The research was performed using computational resources sponsored by the Department of Energy's Office of Energy Efficiency and Renewable Energy and located at the National Renewable Energy Laboratory.

■ REFERENCES

(1) Zevalkink, A.; et al. A practical field guide to thermoelectrics: Fundamentals, synthesis, and characterization. *Appl. Phys. Rev.* **2018**, *5*, 021303.
(2) Toberer, E. S.; May, A. F.; Snyder, G. J. Zintl chemistry for designing high efficiency thermoelectric materials. *Chem. Mater.* **2010**, *22*, 624−634.
(3) Kauzlarich, S. M.; Brown, S. R.; Snyder, G. J. Zintl phases for thermoelectric devices. *Dalton Trans* **2007**, 2099−2107.
(4) Toberer, E. S.; Zevalkink, A.; Snyder, G. J. Phonon engineering through crystal chemistry. *J. Mater. Chem.* **2011**, *21*, 15843−15852.
(5) Beekman, M.; Morelli, D. T.; Nolas, G. S. Better thermoelectrics through glass-like crystals. *Nat. Mater.* **2015**, *14*, 1182−1185.
(6) Kuznetsov, V.; Kuznetsova, L.; Kaliazin, A.; Rowe, D. Preparation and thermoelectric properties of $A_8^{II}B_{16}^{III}B_{30}^{IV}$ clathrate compounds. *J. Appl. Phys.* **2000**, *87*, 7871−7875.
(7) Blake, N. P.; Möllnitz, L.; Kresse, G.; Metiu, H. Why clathrates are good thermoelectrics: A theoretical study of $Sr_8Ga_{16}Ge_{30}$. *J. Chem. Phys.* **1999**, *111*, 3133−3144.
(8) Nolas, G.; Cohn, J.; Slack, G.; Schujman, S. Semiconducting Ge clathrates: Promising candidates for thermoelectric applications. *Appl. Phys. Lett.* **1998**, *73*, 178−180.
(9) Iversen, B. B.; Palmqvist, A. E.; Cox, D. E.; Nolas, G. S.; Stucky, G. D.; Blake, N. P.; Metiu, H. Why are clathrates good candidates for thermoelectric materials? *J. Solid State Chem.* **2000**, *149*, 455−458.
(10) Takabatake, T.; Suekuni, K.; Nakayama, T.; Kaneshita, E. Phonon-glass electron-crystal thermoelectric clathrates: Experiments and theory. *Rev. Mod. Phys.* **2014**, *86*, 669−716.
(11) Christensen, M.; Johnsen, S.; Iversen, B. B. Thermoelectric clathrates of type I. *Dalton Trans* **2010**, *39*, 978−992.
(12) Kleinke, H. New bulk materials for thermoelectric power generation: clathrates and complex antimonides. *Chem. Mater.* **2010**, *22*, 604−611.
(13) Dolyniuk, J.-A.; Owens-Baird, B.; Wang, J.; Zaikina, J. V.; Kovnir, K. Clathrate thermoelectrics. *Mater. Sci. Eng., R* **2016**, *108*, 1−46.
(14) Wang, J.; Lebedev, O. I.; Lee, K.; Dolyniuk, J.-A.; Klavins, P.; Bux, S.; Kovnir, K. High-efficiency thermoelectric $Ba_8Cu_{14}Ge_6P_{26}$: bridging the gap between tetrel-based and tetrel-free clathrates. *Chem. Sci.* **2017**, *8*, 8030−8038.
(15) Saramat, A.; Svensson, G.; Palmqvist, A.; Stiewe, C.; Müller, E.; Platzek, D.; Williams, S.; Rowe, D.; Bryan, J.; Stucky, G. Large thermoelectric figure of merit at high temperature in Czochralski-grown clathrate $Ba_8Ga_{16}Ge_{30}$. *J. Appl. Phys.* **2006**, *99*, 023708.
(16) Wei, P.; Zhao, W.-Y.; Dong, C.-L.; Yang, X.; Yu, J.; Zhang, Q.-J. Excellent performance stability of Ba and In double-filled skutterudite thermoelectric materials. *Acta Mater.* **2011**, *59*, 3244−3254.
(17) Nolas, G.; Morelli, D.; Tritt, T. M. Skutterudites: A phonon-glass-electron crystal approach to advanced thermoelectric energy conversion applications. *Annu. Rev. Mater. Sci.* **1999**, *29*, 89−116.
(18) Nolas, G.; Kaeser, M.; Littleton IV, R.; Tritt, T. High figure of merit in partially filled ytterbium skutterudite materials. *Appl. Phys. Lett.* **2000**, *77*, 1855−1857.
(19) Sales, B.; Mandrus, D.; Williams, R. K. Filled skutterudite antimonides: a new class of thermoelectric materials. *Science* **1996**, *272*, 1325−1328.
(20) Fornari, M.; Singh, D. J. Electronic structure and thermoelectric prospects of phosphide skutterudites. *Phys. Rev. B: Condens. Matter Mater. Phys.* **1999**, *59*, 9722−9724.
(21) Tang, Y.; Qiu, Y.; Xi, L.; Shi, X.; Zhang, W.; Chen, L.; Tseng, S.-M.; Chen, S.-w.; Snyder, G. J. Phase diagram of In−Co−Sb system and thermoelectric properties of In-containing skutterudites. *Energy Environ. Sci.* **2014**, *7*, 812−819.
(22) Tang, Y.; Hanus, R.; Chen, S.-w.; Snyder, G. J. Solubility design leading to high figure of merit in low-cost Ce-$CoSb_3$ skutterudites. *Nat. Commun.* **2015**, *6*, 7584.
(23) Rogl, G.; Rogl, P. Skutterudites, a most promising group of thermoelectric materials. *Curr. Opin. Green Sustain. Chem.* **2017**, *4*, 50−57.
(24) Zong, P.-a.; Hanus, R.; Dylla, M.; Tang, Y.; Liao, J.; Zhang, Q.; Snyder, G. J.; Chen, L. Skutterudite with graphene-modified grain-boundary complexion enhances zT enabling high-efficiency thermoelectric device. *Energy Environ. Sci.* **2017**, *10*, 183−191.
(25) Zhang, Q.; Zhou, Z.; Dylla, M.; Agne, M. T.; Pei, Y.; Wang, L.; Tang, Y.; Liao, J.; Li, J.; Bai, S.; Jiang, W.; Chen, L.; Snyder, G. J. Realizing high-performance thermoelectric power generation through grain boundary engineering of skutterudite-based nanocomposites. *Nano Energy* **2017**, *41*, 501−510.
(26) Brown, S. R.; Kauzlarich, S. M.; Gascoin, F.; Snyder, G. J. $Yb_{14}MnSb_{11}$: New high efficiency thermoelectric material for power generation. *Chem. Mater.* **2006**, *18*, 1873−1877.
(27) Cox, C. A.; Brown, S. R.; Snyder, G. J.; Kauzlarich, S. M. Effect of Ca doping on the thermoelectric performance of $Yb_{14}MnSb_{11}$. *J. Electron. Mater.* **2010**, *39*, 1373−1375.
(28) Toberer, E. S.; Cox, C. A.; Brown, S. R.; Ikeda, T.; May, A. F.; Kauzlarich, S. M.; Snyder, G. J. Traversing the metal-insulator transition in a Zintl phase: rational enhancement of thermoelectric efficiency in $Yb_{14}Mn_{1-x}Al_xSb_{11}$. *Adv. Funct. Mater.* **2008**, *18*, 2795−2800.
(29) Toberer, E. S.; Zevalkink, A.; Crisosto, N.; Snyder, G. J. The Zintl compound $Ca_5Al_2Sb_6$ for low-cost thermoelectric power generation. *Adv. Funct. Mater.* **2010**, *20*, 4375−4380.
(30) Zevalkink, A.; Toberer, E. S.; Bleith, T.; Flage-Larsen, E.; Snyder, G. J. Improved carrier concentration control in Zn-doped $Ca_5Al_2Sb_6$. *J. Appl. Phys.* **2011**, *110*, 013721.
(31) Zevalkink, A.; Zeier, W. G.; Pomrehn, G.; Schechtel, E.; Tremel, W.; Snyder, G. J. Thermoelectric properties of Sr_3GaSb_3−a chain-forming Zintl compound. *Energy Environ. Sci.* **2012**, *5*, 9121−9128.
(32) Zevalkink, A.; Toberer, E. S.; Zeier, W. G.; Flage-Larsen, E.; Snyder, G. J. Ca 3 AlSb 3: an inexpensive, non-toxic thermoelectric material for waste heat recovery. *Energy Environ. Sci.* **2011**, *4*, 510−518.
(33) Zeier, W. G.; Zevalkink, A.; Schechtel, E.; Tremel, W.; Snyder, G. J. Thermoelectric properties of Zn-doped Ca_3AlSb_3. *J. Mater. Chem.* **2012**, *22*, 9826−9830.
(34) Zevalkink, A.; Pomrehn, G.; Takagiwa, Y.; Swallow, J.; Snyder, G. J. Thermoelectric Properties and Electronic Structure of the Zintl-Phase Sr_3AlSb_3. *ChemSusChem* **2013**, *6*, 2316−2321.

(35) Aydemir, U.; Zevalkink, A.; Ormeci, A.; Gibbs, Z. M.; Bux, S.; Snyder, G. J. Thermoelectric enhancement in $BaGa_2Sb_2$ by Zn doping. *Chem. Mater.* **2015**, *27*, 1622−1630.
(36) Gascoin, F.; Ottensmann, S.; Stark, D.; Haïle, S. M.; Snyder, G. J. Zintl phases as thermoelectric materials: tuned transport properties of the compounds $Ca_xYb_{1-x}Zn_2Sb_2$. *Adv. Funct. Mater.* **2005**, *15*, 1860−1864.
(37) Fleurial, J.-P.; Bux, S.; Caillat, T. Engineering of novel thermoelectric materials and devices for next generation, long life, 20% efficient space power systems. *11th International Energy Conversion Engineering Conference*; 2013; p 3927.
(38) Madsen, G. K. Automated search for new thermoelectric materials: the case of LiZnSb. *J. Am. Chem. Soc.* **2006**, *128*, 12140−12146.
(39) Toberer, E. S.; May, A. F.; Scanlon, C. J.; Snyder, G. J. Thermoelectric properties of p-type LiZnSb: Assessment of ab initio calculations. *J. Appl. Phys.* **2009**, *105*, 063701.
(40) Gorai, P.; Goyal, A.; Toberer, E. S.; Stevanović, V. A simple chemical guide for finding novel n-type dopable Zintl pnictide thermoelectric materials. *J. Mater. Chem. A* **2019**, *7*, 19385−19395.
(41) Ohno, S.; Aydemir, U.; Amsler, M.; Pöhls, J.-H.; Chanakian, S.; Zevalkink, A.; White, M. A.; Bux, S. K.; Wolverton, C.; Snyder, G. J. Achieving zT > 1 in inexpensive zintl phase $Ca_9Zn_{4+x}Sb_9$ by phase boundary mapping. *Adv. Funct. Mater.* **2017**, *27*, 1606361.
(42) Ohno, S.; Imasato, K.; Anand, S.; Tamaki, H.; Kang, S. D.; Gorai, P.; Sato, H. K.; Toberer, E. S.; Kanno, T.; Snyder, G. J. Phase boundary mapping to obtain n-type Mg_3Sb_2-based thermoelectrics. *Joule* **2018**, *2*, 141−154.
(43) Ortiz, B. R.; Gordiz, K.; Gomes, L.; Braden, T.; Adamczyk, J. M.; Qu, J.; Ertekin, E.; Toberer, E. S. Carrier density control in $Cu_2HgGeTe_4$ and discovery of Hg_2GeTe_4 via phase boundary mapping. *J. Mater. Chem. A* **2019**, *7*, 621−631.
(44) Crawford, C. M.; Ortiz, B. R.; Gorai, P.; Stevanovic, V.; Toberer, E. S. Experimental and Computational Phase Boundary Mapping of $Co_4Sn_6Te_6$. *J. Mater. Chem. A* **2018**, *6*, 24175−24185.
(45) Zhang, J.; Song, L.; Sist, M.; Tolborg, K.; Iversen, B. B. Chemical bonding origin of the unexpected isotropic physical properties in thermoelectric Mg_3Sb_2 and related materials. *Nat. Commun.* **2018**, *9*, 4716.
(46) Ortiz, B. R.; Gorai, P.; Stevanovic, V.; Toberer, E. S. Thermoelectric performance and defect chemistry in n-type Zintl $KGaSb_4$. *Chem. Mater.* **2017**, *29*, 4523−4534.
(47) Ortiz, B. R.; Gorai, P.; Krishna, L.; Mow, R.; Lopez, A.; McKinney, R.; Stevanović, V.; Toberer, E. S. Potential for high thermoelectric performance in n-type Zintl compounds: a case study of Ba doped KAlSb 4. *J. Mater. Chem. A* **2017**, *5*, 4036−4046.
(48) Kim, S.-J.; Kanatzidis, M. G. A unique framework in $BaGa_2Sb_2$: a new Zintl phase with large tunnels. *Inorg. Chem.* **2001**, *40*, 3781−3785.
(49) Cordier, G.; Ochmann, H. Crystal structure of potassium tecto-tetraantimonidoaluminate, $KAlSb_4$. *Z. Kristallogr. Cryst. Mater.* **1991**, *195*, 308−309.
(50) Cordier, G.; Ochmann, H. Crystal structure of potassium tecto-tetraantimonidogallate, $KGaSb_4$. *Z. Kristallogr. Cryst. Mater.* **1991**, *195*, 306−307.
(51) Oszlányi, G.; Sütő, A. Ab initio structure solution by charge flipping. *Acta Crystallogr., Sect. A: Found. Crystallogr.* **2004**, *60*, 134−141.
(52) Oszlányi, G.; Sütő, A. Ab initio structure solution by charge flipping. II. Use of weak reflections. *Acta Crystallogr., Sect. A: Found. Crystallogr.* **2005**, *61*, 147−152.
(53) Oszlányi, G.; Sütő, A.; Czugler, M.; Párkányi, L. Charge flipping at work: A case of pseudosymmetry. *J. Am. Chem. Soc.* **2006**, *128*, 8392−8393.
(54) Coelho, A. A charge-flipping algorithm incorporating the tangent formula for solving difficult structures. *Acta Crystallogr., Sect. A: Found. Crystallogr.* **2007**, *63*, 400−406.
(55) Kresse, G.; Furthmüller, J. Efficient Iterative Schemes for Ab Initio Total-Energy Calculations Using a Plane-Wave Basis Set. *Phys. Rev. B: Condens. Matter Mater. Phys.* **1996**, *54*, 11169−11186.
(56) Perdew, J. P.; Burke, K.; Ernzerhof, M. Generalized Gradient Approximation Made Simple. *Phys. Rev. Lett.* **1996**, *77*, 3865−3868.
(57) Yan, J.; Gorai, P.; Ortiz, B.; Miller, S.; Barnett, S. A.; Mason, T.; Stevanovic, V.; Toberer, E. S. Material descriptors for predicting thermoelectric performance. *Energy Environ. Sci.* **2015**, *8*, 983−994.
(58) Miller, S. A.; Gorai, P.; Ortiz, B. R.; Goyal, A.; Gao, D.; Barnett, S. A.; Mason, T. O.; Snyder, G. J.; Lv, Q.; Stevanovic, V.; Toberer, E. S. Capturing Anharmonicity in a Lattice Thermal Conductivity Model for High-Throughput Predictions. *Chem. Mater.* **2017**, *29*, 2494−2501.
(59) Stevanović, V.; Lany, S.; Zhang, X.; Zunger, A. Correcting Density Functional Theory for Accurate Predictions of Compound Enthalpies of Formation: Fitted Elemental-Phase Reference Energies. *Phys. Rev. B: Condens. Matter Mater. Phys.* **2012**, *85*, 115104.
(60) Blöchl, P. E. Projector Augmented-Wave Method. *Phys. Rev. B: Condens. Matter Mater. Phys.* **1994**, *50*, 17953−17979.
(61) Peng, H.; Scanlon, D. O.; Stevanović, V.; Vidal, J.; Watson, G. W.; Lany, S. Convergence of Density and Hybrid Functional Defect Calculations for Compound Semiconductors. *Phys. Rev. B: Condens. Matter Mater. Phys.* **2013**, *88*, 115201.
(62) Lany, S.; Zunger, A. Accurate Prediction of Defect Properties in Density Functional Supercell Calculations. *Modell. Simul. Mater. Sci. Eng.* **2009**, *17*, 084002.
(63) Goyal, A.; Gorai, P.; Peng, H.; Lany, S.; Stevanović, V. A Computational Framework for Automation of Point Defect Calculations. *Comput. Mater. Sci.* **2017**, *130*, 1−9.
(64) Cordier, G.; Ochmann, H. Crystal structure of dicaesium catena-diantimonidogallate, Cs_2GaSb_2. *Z. Kristallogr. Cryst. Mater.* **1991**, *195*, 310−311.
(65) Park, S.-M.; Kim, S.-J.; Kanatzidis, M. G. Ga−Ga bonding and tunnel framework in the new Zintl phase $Ba_3Ga_4Sb_5$. *J. Solid State Chem.* **2003**, *175*, 310−315.
(66) Kim, S.-J.; Hu, S.; Uher, C.; Kanatzidis, M. G. $Ba_4In_8Sb_{16}$: Thermoelectric properties of a new layered Zintl phase with infinite zigzag Sb chains and pentagonal tubes. *Chem. Mater.* **1999**, *11*, 3154−3159.
(67) Cordier, G.; Ochmann, H. Crystal structure of potassium phyllodiantimonidogallate, $KGaSb_2$. *Z. Kristallogr. - Cryst. Mater.* **1991**, *197*, 297−298.
(68) Cordier, G.; Ochmann, H.; Schäfer, H. vur isosterie bei halbmetallanionen: Dem $(BS2)_\infty$ isostere $GaSb_2^{2-}$ anionen IM K_2GaSb_2. *J. Less-Common Met.* **1986**, *119*, 291−296.
(69) Cordier, G.; Ochmann, H. Crystal structure of dipotassium phyllotriantimonidodigallate, $K_2Ga_2Sb_3$. *Z. Kristallogr. - Cryst. Mater.* **1991**, *197*, 289−290.
(70) Schäfer, M. C.; Bobev, S. Tin clathrates with the type II structure. *J. Am. Chem. Soc.* **2013**, *135*, 1696−1699.

https://dx.doi.org/10.1021/acsaem.0c00048
ACS Appl. Energy Mater. 2020, 3, 2182−2191